N. E. May
Aircraft Research Association Ltd.,
Manton Lane,
Bedford MK41 7PF United Kingdom

J. W. Chew
Rolls-Royce Ltd.,
PO Box 31,
Derby DE2 8BJ United Kingdom

P. W. James
Polytechnic South West,
Drake Circus,
Plymouth PL4 8AA United Kingdom

Calculation of Turbulent Flow for an Enclosed Rotating Cone

Prediction of the flow in the cavity between a rotating cone and an outer stationary cone with and without throughflow is considered. A momentum-integral method and a finite difference method for solution of the Reynolds-averaged Navier–Stokes equations with a mixing-length model of turbulence are applied. These two methods have previously been validated for flow between corotating and rotor–stator disk systems, but have not been properly tested for conical systems. Both methods have been evaluated by comparing predictions with the experimental measurements of other workers. There is good agreement for cone half-angles greater than or equal to 60 deg but discrepancies are evident for smaller angles. "Taylor-type" vortices, the existence of which has been postulated by other workers and which are not captured by the present steady, axisymmetric models, may contribute to these discrepancies.

1 Introduction

The need to improve design methods for turbomachinery has led to considerable effort being put into the development of predictive techniques for the flow in turbine and compressor disk cavities. Despite the variety of geometries of this type that occur in gas turbine engines, most predictive methods have been validated only for relatively simple plane disk geometries. In the present paper two predictive techniques that have been previously validated using data for turbulent flow in rotating disk cavities are evaluated using data for a shrouded rotating cone. The objective of this work is to clarify the range of validity of current methods and identify any particular problems associated with the conical geometry.

For a review of predictive methods for rotating disk flows the interested reader is referred to Chew (1990). However, to put the present contributions in context it is appropriate to mention some of the previous work on predictive methods. The earliest relevant publication is perhaps that of von Karman (1921). Von Karman derived a momentum-integral solution for turbulent flow induced by a disk rotating in a quiescent environment (the "free disk" problem). Many workers have subsequently used similar momentum-integral methods for a variety of rotating disk flows and the technique remains popular because of its computational efficiency and convenience in analysis. Relatively recent applications of the momentum-integral method include radial outflow and inflow between corotating disks (Owen et al., 1985; Chew and Rogers, 1988; Farthing et al., 1991) and flow in rotor–stator disk systems with or without an imposed throughflow (Owen and Rogers, 1989; Chew, 1991).

Over the last decade or so use of finite difference methods to solve the Reynolds-averaged Navier–Stokes equations for rotating disk flows has become increasingly popular. Some difficulties have been encountered both with turbulence modeling and with numerical algorithms, but it has now been demonstrated that a variety of turbulence models and numerical schemes can be successfully applied to rotating disk flows. Examples for corotating disk systems are given by Chew (1985) and Morse (1988), and for rotor–stator disk systems by Chew and Vaughan (1988), Roscoe et al. (1988), and Morse (1991).

In contrast to the disk problem, the rotating cone has received little attention. Tien (1960) showed that under laminar boundary layer assumptions the laminar free disk solution can be applied to the free cone problem. Kreith (1966) applied von Karman's momentum-integral method to the turbulent free cone problem and, as shown below, with appropriate nondimensionalization, the momentum-integral equations become identical to those for the free disk. Koosinlin et al. (1974) applied boundary layer finite difference methods, with a mixing-length turbulence model, to flow on a spinning cone with and without an imposed axial flow. The authors are not aware of any previous attempts to predict the flow for the problem considered here, namely the enclosed rotating cone with throughflow.

The two predictive methods that have been adopted here for the rotating cone problem are a von Karman-type momentum-integral method and the finite difference method of Vaughan et al. (1989), which uses a mixing-length model of turbulence. The momentum-integral method is developed from that applied previously to rotor–stator disk cavities and the turbulence model, which has been validated against data for free disks and cones, corotating disk cavities, and rotor–stator disk systems, is based on that of Koosinlin et al. These two methods are described in Sections 2 and 3 below. Comparison of theoretical predictions with the experimental results for moment coefficient of Yamada and Ito (1975, 1979) are then given in

Contributed by the International Gas Turbine Institute and presented at the 37th International Gas Turbine and Aeroengine Congress and Exposition, Cologne, Germany, June 1–4, 1992. Manuscript received by the International Gas Turbine Institute February 4, 1992. Paper No. 92-GT-70. Associate Technical Editor: L. S. Langston.

Section 4. Also included in Section 4 is a comparison of the finite difference predictions with the measurements of Bilgen and Boulous (1973) for an enclosed rotating cylinder, as this flow configuration could be considered a limiting case of the cone problem. The conclusions from the present study are summarized in Section 5.

2 The Momentum-Integral Method

2.1 Assumptions. The geometry of the rotor–stator cone system considered and the assumed flow structure are shown in Fig. 1. The outer and inner radii of the cones are b and a, respectively. The perpendicular distance between the rotor and stator is denoted by d. The rotor is rotating about an axis at $r = 0$ with constant angular velocity Ω and the orthogonal coordinate system (s, θ, n), shown in Fig. 1, is used. The cone half-angle is denoted by λ and the nondimensional mass throughflow rate (which may be zero) is denoted by Cq. Throughout this paper, the flow is assumed to be turbulent and flow variables are assumed to have been averaged over a suitably large time scale, so that they denote turbulent mean quantities. The components of velocity are denoted by (u, v, w), the pressure by p, and the density by ρ.

The flow pattern shown in Fig. 1 is postulated assuming that the flow develops in a similar way to that in rotor–stator disk systems. The pattern occurring in rotor–stator disk systems has been confirmed by experimental work (see, for example, Daily and Nece, 1960; Daily et al., 1964) and by finite difference results (see, for example, Chew and Vaughan, 1988). In the "source" region, fluid is entrained into a boundary layer on the rotor; any flow on the stator up to this point is neglected. Outside the source region fluid is "centrifuged" radially outward in a boundary layer on the rotor and radially inward along the stator. Flow is channeled into the stator boundary layer through a boundary layer on the shroud. Between these boundary layers there is a core where there is a weak axial velocity toward the rotor and negligible radial velocity. The

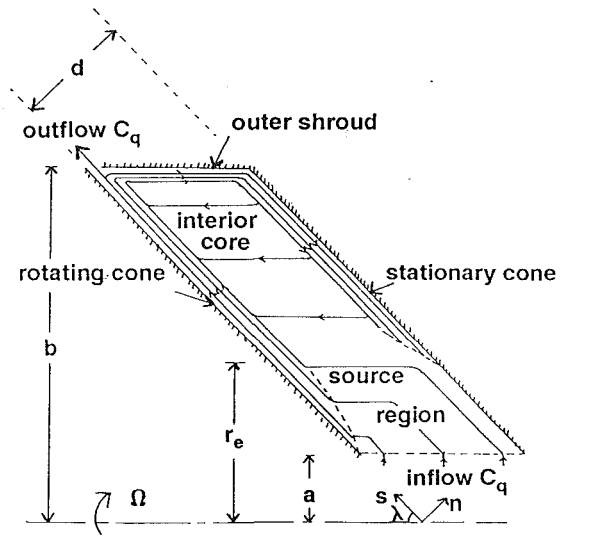

Fig. 1 Postulated flow pattern in rotor–stator cone system (⟶ typical streamline, ····· boundary layer edge)

Nomenclature

a = inner radius
b = outer radius
Cm = moment coefficient = $2M \sin \lambda/\rho\Omega^2 b^5$
Cm' = moment coefficient = $2M/\pi\rho\Omega^2 b^4 t$
Cq = nondimensional mass throughflow rate = $\dot{m}/\mu b$
d = perpendicular distance between rotor and stator
F = friction factor
$F_i(\bar{V})$ = see Eqs. (16) and (17)
I_1, I_2, I_3, I_4, I_5 = constants obtained by integrating velocity profiles across the boundary layer (see Section 2.2)
l = mixing length
$\dot{m}$ = mass flow rate
$\dot{m}_b$ = mass flow rate in shroud boundary layer
M = moment exerted on rotor
n = normal coordinate direction in "tilted" cylindrical polar coordinate system
$p(s, n)$ = static pressure
r = radial coordinate direction in cylindrical polar coordinate system
r_e = radial location of end of source region
Re = Reynolds number used by Yamada and Ito = $\Omega b^2/\nu$
Re_θ = Reynolds number used in integral method = $\Omega b^2/\nu \sin \lambda$
s = coordinate direction parallel to cone in "tilted" cylindrical polar system
t = length of cylinder
$u(s, n)$ = s-velocity component
$\hat{u}(s)$ = s-dependent component of $u(s, n)$
$u_1(x)$ = nondimensionalized $u(s) = u/\Omega r_o$
$v(s, n)$ = tangential velocity component
$\bar{V}(x)$ = nondimensionalized boundary layer edge tangential velocity = $\bar{v}/\Omega r_o$
$V_b(z)$ = bulk tangential velocity in shroud boundary layer
$V_o(x)$ = nondimensionalized surface tangential velocity = $v_o/\Omega r_o$
$w(s, n)$ = n-velocity component
x = nondimensional distance = r_o/b
x_n = normal distance from surface
Y_1 = dependent variable used in integral method = $u_1\delta_1 x^3$
Y_2 = dependent variable used in integral method = $\delta_1 x$
z = coordinate direction in cylindrical polar coordinate system
$\delta(s)$ = boundary layer thickness
$\delta_1(x)$ = nondimensional boundary layer thickness = $\mathrm{Re}_\theta^{1/5} \sin \lambda\, \delta/r_o$
θ = tangential coordinate in cylindrical and "tilted" cylindrical polar coordinate systems
λ = cone half angle
μ = laminar dynamic viscosity
$\mu_e(s, n)$ = effective dynamic viscosity = $\mu + \mu_t$
$\mu_t(s, n)$ = turbulent dynamic viscosity
ν = laminar kinematic viscosity = μ/ρ
ρ = density
$\tau_{ij}(s, n)$ = stress components, where i and j represent s, θ, or n
$\tau_W(s)$ = resultant wall shear stress
ω = under-relaxation factor (Eq. (18))
Ω = angular velocity of rotor

Subscripts

o = value on rotor or stator surface

Superscripts

s = stator variable
$\bar{}$ = values at the boundary layer edge

flow throughout the cavity is assumed to be incompressible, steady, and axisymmetric and the flow external to the boundary layers in both the source region and the core region will be treated as inviscid.

The application of boundary layer assumptions to the Navier-Stokes equations for the conical geometry is similar to that for disk systems but requires the additional assumption

$$s \sin \lambda \gg n \cos \lambda. \tag{1}$$

The physical interpretation of this assumption is that the change in radius across the boundary layer is small compared with the local radius. May (1990) has confirmed numerically that this assumption is appropriate for the conditions considered here.

Applying the usual boundary layer assumptions, along with the above assumption, to the Reynolds-averaged Navier-Stokes equations, the following boundary layer equations are obtained:

$$\frac{1}{r}\frac{\partial}{\partial s}(\rho r u) + \frac{1}{r}\frac{\partial}{\partial n}(\rho r w) = 0, \tag{2}$$

$$\frac{1}{r}\frac{\partial}{\partial s}(\rho r u^2) + \frac{1}{r}\frac{\partial}{\partial n}(\rho r u w) - \frac{\rho v^2}{r}\sin\lambda + \frac{\partial p}{\partial s} = \frac{1}{r}\frac{\partial}{\partial n}(r\tau_{sn}), \tag{3}$$

$$\frac{1}{r^2}\frac{\partial}{\partial s}(\rho r^2 u v) + \frac{1}{r}\frac{\partial}{\partial n}(\rho r w v) = \frac{1}{r^2}\frac{\partial}{\partial n}(r^2\tau_{\theta n}), \tag{4}$$

$$\frac{\partial p}{\partial n} = 0. \tag{5}$$

The shear stresses τ_{sn} and $\tau_{\theta n}$ in these equations represent the sum of the laminar and Reynolds stresses.

2.2 Rotor Boundary Layer. The velocity profiles and surface shear stress formulae used for the rotor boundary layer at $n = 0$ are the following generalizations of those used by von Karman:

$$v(s, n) = \bar{v}(s) - (\bar{v}(s) - v_0(s))[1 - (n/\delta)^{1/7}], \tag{6}$$

$$u(s, n) = \tilde{u}(s)\,(n/\delta)^{1/7}(1 - n/\delta), \tag{7}$$

$$\tau_{\theta n,o} = -0.0225\rho(\nu/\delta)^{1/4}(v_0 - \bar{v})[\tilde{u}^2 + (v_0 - \bar{v})^2]^{3/8}, \tag{8}$$

$$\tau_{sn,o} = -\frac{\tilde{u}}{v_0 - \bar{v}}\,\tau_{\theta n,o}. \tag{9}$$

In Eqs. (6)-(9), δ is the boundary layer thickness, ν is the kinematic viscosity, the subscript 0 denotes wall value, and the overbar represents values at the boundary layer edge.

Using Eqs. (6)-(9), Eqs. (2)-(5) may be integrated from $n = 0$ to $n = \delta$ and the resulting equations combined to give two momentum integral equations. These two equations, when nondimensionalized by the substitutions

$$x = \frac{r_0}{b}, \quad u_1 = \frac{\tilde{u}}{\Omega r_0}, \quad \bar{V} = \frac{\bar{v}}{\Omega r_0},$$

$$V_0 = \frac{v_0}{\Omega r_0}, \quad \delta_1 = \frac{\delta}{r_0}\,\mathrm{Re}_\theta^{1/5}\sin\lambda, \quad \mathrm{Re}_\theta = \frac{\Omega b^2}{\nu \sin\lambda}, \tag{10}$$

are

$$2I_4 Y_1 Y_2 \frac{dY_1}{dx} - I_4 Y_1^2 \frac{dY_2}{dx} =$$

$$-0.0225\,Y_1 x^{7/4}\left[\left(\frac{Y_1}{x^2}\right)^2 + Y_2^2(V_0 - \bar{v})^2\right]^{3/8}$$

$$+\frac{Y_1^2 Y_2}{x} I_4 - (Y_2 x)^3[2\bar{V}(\bar{V} - V_0)I_2 - (\bar{V} - V_0)^2 I_5], \tag{11}$$

$$I_3 Y_2 \frac{dY_1}{dx} = 0.0225 x^{7/4}\left[\left(\frac{Y_1}{x_2}\right)^2 + Y_2^2(V_0 - \bar{V})^2\right]^{3/8}$$

$$-\frac{(I_1 - I_3)}{(V_0 - \bar{V})} Y_1 Y_2 \frac{d\bar{V}}{dx} - \frac{2Y_1 Y_2}{x(V_0 - \bar{V})}[I_1\bar{V} + I_3(V_0 - \bar{V})]. \tag{12}$$

Here $Y_1 = u_1\delta_1 x^3$ and $Y_2 = \delta_1 x$. The constants I_1 to I_5 in Eqs. (11) and (12) arise from the integration of the power law velocity profiles and are given by $I_1 = 49/120$, $I_2 = 1/8$, $I_3 = 49/720$, $I_4 = 343/1656$, and $I_5 = 1/36$. It may be noted that Eqs. (11) and (12), and their initial conditions (see Section 2.5), are independent of λ, and so their solutions are also independent of cone half angle. However, as will be seen from results presented in Section 4, the validity of the assumptions underlying the equations may well depend on cone half-angle λ.

2.3 Stator Boundary Layer. The equations describing the flow in the stator boundary layer are the same as those derived by Chew (1991) for rotor-stator disk systems. This model is based on finite difference predictions for a disk system, which show that the tangential velocity profile (Eq. (6) with $v_0 = 0$) gives a reasonable representation of the flow on the stator, whereas the s-velocity profile (Eq. (7)) gives a poor representation. In a further finite difference study (May, 1990) it was shown that the conclusions for the disk system also applied to rotor-stator cone systems with λ as small as 15 deg. As in the disk flow work the following equations are used for the stator boundary layer:

$$u_1^s = -0.364\bar{V}^s, \tag{13}$$

$$\frac{dY_2^s}{dx} = \frac{Y_2^s}{x} - \frac{0.0648}{I_3^s(\bar{V}^s Y_2^s x)^{1/4}} + \frac{Y_2^s}{x}\frac{(2I_1^s - 5I_3^s)}{I_3^s}$$

$$-\frac{d\bar{V}^s}{dx}\frac{Y_2^s}{\bar{V}^s}\left(\frac{2I_3^s - I_1^s}{I_3^s}\right), \tag{14}$$

where $I_1^s = I_1$, $I_3^s = I_3/2$ and the superscript s denotes evaluation for the stator boundary layer. Equation (14) expresses conservation of angular momentum. Equation (13) is based on an examination of finite difference predictions, which showed that the velocity vector of the flow close to the stator surface is at an angle of about 20 deg to the tangential direction. However, as described by May (1990), the value of the limiting flow angle becomes more erratic for cases with throughflow and the assumption that it is always 20 deg becomes questionable. In an attempt to avoid the use of the limiting flow angle, momentum integral equations were derived by May (1990) using radial and tangential velocity profiles that more closely match the finite difference results. However, the equations were more complex than Eq. (14) and the results obtained did not show sufficient improvement to justify their use.

2.4 Shroud Treatment. The shroud channels fluid from the rotor boundary layer into the stator boundary layer, as shown in Fig. 1. Constant mass flow rate ($\dot{m}_b$) and friction factor, F, are assumed in this thin layer, as in the disk flow model. Conservation of angular momentum in the shroud layer then gives the equation

$$\dot{m}_b \frac{dV_b}{dz} = 2\pi b \frac{F}{2}\rho V_b^2, \tag{15}$$

where V_b is the bulk tangential velocity and $z = n \sin\lambda - s\cos\lambda$. Equation (15) may be integrated directly to obtain $\bar{V}^s$ at $x = 1$ from the rotor boundary layer solution at $x = 1$.

2.5 Solution Method. The solutions of the boundary layer equations for the rotor and stator are coupled through the shroud boundary layer and the inviscid flow region. The ordinary differential Eqs. (11), (12), and (14) were solved using

a variable order, variable step-length Numerical Algorithms Group (NAG) library routine for the solution of a stiff system of ordinary differential equations.

In the source region, between $r = a$ and $r = r_e$, (see Fig. 1), $\overline{V}(x)$ is given by the free vortex relation $r\overline{V} = \text{const}$, which expresses conservation of angular momentum external to the rotor boundary layer. Equations (11) and (12) are then integrated from $x = a/b$ to find Y_1 and Y_2. The initial conditions for Y_1 and Y_2 are $Y_1 = Y_2 = 0$ at $x = a/b$, corresponding to zero mass flow rate and zero boundary layer thickness. In practice, to avoid singularities in Eqs. (11) and (12), Y_1 and Y_2 were given initial values of 10^{-10}. The end of the source region is defined as the point at which all the inlet throughflow has been entrained into the rotor boundary layer. Any boundary layer flow on the stator in the source region is neglected.

In the core region, it is assumed that both the radial velocity component and the axial gradient of tangential velocity are zero (i.e., $\overline{V}(x) = \overline{V}^s(x)$) in the inviscid region between the boundary layers. An iterative solution procedure is used to find solutions to Eqs. (11), (12), and (14), which satisfy conservation of mass within the cavity. The velocity $\overline{V}(x)$ is specified at N points x_i ($i = 1, \ldots, N$), equally spaced (radially) in the core region with $x_1 = r_e/b$ and $x_N = 1$. A cubic spline curve fit is then used to interpolate $\overline{V}(x)$ between these points. Using a specified $\overline{V}$ distribution, the rotor equations may be solved from $x = r_e/b$ to $x = 1$, using the solutions from the end of the source region as initial conditions. From a mass balance at $x = 1$, initial conditions may be obtained for the stator equation, which is then solved from $x = 1$ to $x = r_e/b$. The solutions thus obtained are then fed into mass balance equations at each radial location, giving rise to a set of $(N - 1)$ nonlinear simultaneous equations of the form

$$F_i(\overline{V}) = \frac{Y_1 - Y_1^s - Cq/(2\pi I_1 \,\mathrm{Re}_\theta^{4/5})}{Y_1} = 0, \quad i = 1, \ldots, (N-1). \tag{16}$$

A final equation at $x = 1$ is obtained from the shroud condition:

$$F_N(\overline{V}) = \frac{\overline{V}^s(1) - \overline{V}(1)}{\overline{V}(1)} = 0. \tag{17}$$

The $\overline{V}$ distribution is updated iteratively as described below and the solution procedure is repeated until max $|F_i(\overline{V})| < T$, where T is a tolerance which, from numerical experiments, was given a value of 0.01.

Several schemes were tried to update the $\overline{V}$ distribution. The best scheme in terms of speed and robustness was found to be one where the values of $\overline{V}(x_i)$ for the jth iteration are calculated from

$$\overline{V}^j(x_i) = \overline{V}^{j-1}(x_i) + \omega \overline{V}^{j-1}(x_i) F_i(\overline{V}). \tag{18}$$

In Eq. (18) ω is an underrelaxation factor, which is normally taken to be 0.5.

A typical run took about 30 iterations to converge and used about 30 seconds processing time on a Prime 6350 computer. Numerical experiments showed that a value of $N = 10$ was sufficient to give grid-independent solutions. This solution scheme is significantly faster than that used by Chew (1991), in which a linear variation of $\overline{V}$ between radial stations was assumed and the resulting equations were solved using a library routine for simultaneous nonlinear equations.

3 The Finite Difference Method

The finite difference code used in this work is a modified version of that written by Vaughan et al. (1989) to investigate flows in rotating disk systems. The modifications involved "tilting" the original plane disk cavity through an arbitrary angle, λ, to produce the computational domain shown in Fig. 2.

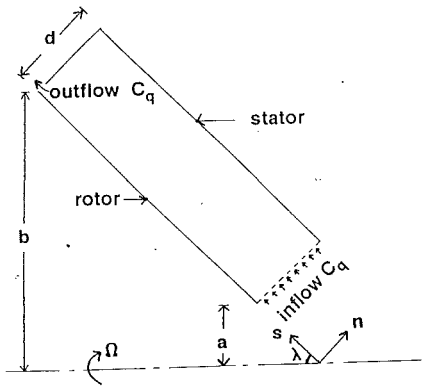

Fig. 2 Solution domain for the tilted rotating cavity

3.1 Governing Equations and Turbulence Model. For steady, axisymmetric flow, the Reynolds-averaged continuity and momentum equations may be written in terms of the (s, θ, n) coordinate system as

$$\frac{\partial}{\partial s}(\rho r u) + \frac{\partial}{\partial n}(\rho r w) = 0, \tag{19}$$

$$\frac{1}{r}\frac{\partial}{\partial s}(\rho r u \phi) + \frac{1}{r}\frac{\partial}{\partial n}(\rho r w \phi) = \frac{1}{r}\frac{\partial}{\partial s}\left[\mu_e \frac{\partial \phi}{\partial s}\right] + \frac{1}{r}\frac{\partial}{\partial n}\left[\mu_e \frac{\partial \phi}{\partial n}\right] + S_\phi, \tag{20}$$

where $\Phi = u$, v, or w. The density is assumed to be constant for the present studies. The source terms S_Φ for the u, v, and w momentum equations are given by

$$S_u = \rho \frac{v^2}{r} \sin\lambda - \frac{\partial p}{\partial s} + \frac{1}{r}\frac{\partial}{\partial s}\left[\mu_e r \frac{\partial u}{\partial s}\right] + \frac{1}{r}\frac{\partial}{\partial n}\left[\mu_e r \frac{\partial w}{\partial s}\right] - 2\frac{\mu_e}{r^2}\sin\lambda(u \sin\lambda + w \cos\lambda), \tag{21}$$

$$S_v = -\rho \frac{wv}{r}\cos\lambda - \rho \frac{uw}{r}\sin\lambda + v\frac{\cos\lambda}{r^2}\frac{\partial}{\partial n}(\mu_e r) - v\frac{\sin\lambda}{r^2}\frac{\partial}{\partial s}(\mu_e r), \tag{22}$$

and

$$S_w = +\rho \frac{v^2}{r}\cos\lambda - \frac{\partial p}{\partial n} + \frac{1}{r}\frac{\partial}{\partial n}\left[\mu_e r \frac{\partial w}{\partial n}\right] + \frac{1}{r}\frac{\partial}{\partial s}\left[\mu_e r \frac{\partial u}{\partial n}\right] - 2\frac{\mu_\theta}{r^2}\cos\lambda(u \sin\lambda + w \cos\lambda). \tag{23}$$

The system of Eqs. (19)–(23) is closed using a mixing-length turbulence model as described by Chew and Vaughan (1988). Briefly, μ_e is calculated as the sum of the laminar viscosity, μ, and a turbulent viscosity, μ_t. The turbulent viscosity is calculated from

$$\mu_t = \rho l^2 \left[\left(\frac{\partial u_p}{\partial x_n}\right)^2 + \left\{r\frac{\partial}{\partial x_n}\left(\frac{v}{r}\right)\right\}^2\right]^{1/2}, \tag{24}$$

where l is the mixing length, u_p is the velocity component parallel to the boundary surface in the s, n plane, and x_h is the direction normal to the surface. Close to the wall,

$$l = 0.42 x_n [1 - \exp\{-x_n(\rho\tau_w)^{1/2}/(26\mu)\}],$$

where τ_w is the wall shear stress, and elsewhere $l = 0.085\delta$. The influence of rotation on mixing length is accounted for by use of a Richardson number correction, as described by Koosinlin et al. (1974) and Chew and Vaughan (1988).

3.2 Numerical Method. The derivation of the finite difference equations from Eqs. (19)–(24) follows the finite volume approach of Patankar (1980) using "hybrid" differencing for the convective terms. An iterative, nonlinear, multigrid method is used to solve the equations on a staggered nonuniform rectangular mesh. The continuity Eq. (19) is used to derive a pressure correction equation following the SIMPLEC formulation of van Doormal and Raithby (1984). Due to the nonlinearity of the equations, underrelaxation factors are used for the three velocity components, pressure, turbulent viscosity, and multigrid corrections.

An additional damping term was included in the radial momentum equation for disk flows by Vaughan et al. (1989). This approach was extended here to both the u and w momentum equations. For further details of the numerical scheme, see Vaughan et al.

A typical run performed on a 65 × 65 grid took about three hours processing time on a Prime 6350.

4 Results

In this section, the moment coefficients Cm, predicted by the integral method of Section 2 and by the finite difference method of Section 3, will be compared with experimental data. The experimental data are those of Yamada and Ito (1975, 1979) who considered the effects of gap width, d/b, Reynolds number, Re (where $\mathrm{Re} = \mathrm{Re}_\theta \sin\lambda$) and throughflow rate, Cq, on Cm for rotor-stator cone systems with $\lambda = 15, 30, 45, 60, 75$, and 90 deg. In addition the data of Bilgen and Boulos (1973) are used to compare the moment coefficient predicted by the finite difference program for a rotor-stator cylinder system (i.e., $\lambda = 0$ deg).

The effect of cone half-angle on moment coefficient is shown in Figs. 3(*a–f*), for $C_q = 0$, where d/b decreases from 0.24 in Fig. 3(*a*) to 0.008 in Fig. 3(*f*). Figures 3(*a–e*) show excellent agreement between the predictions of the integral method and experiment for $\lambda \geq 60$ deg, the relative error always being less than 5 percent. From the same figures it can be seen that the agreement between the integral method predictions and experiment is poor for $\lambda \leq 45$ deg, where it is clear that the integral method is not reproducing the experimental trend. In Fig. 3(*f*), the agreement is poor for all λ, which can be explained by the experimentally observed fact that for such a small gap width the rotor and stator boundary layers are merged. The finite difference predictions shown in Figs. 3(*a–b*) do not show any overall improvement over those of the integral method, the dependence of Cm on λ being similar to that predicted by the integral method. (The differences between the finite difference and integral method results for $\lambda \geq 60$ deg may, in part, be attributed to the influence of the different solution domains near the outer shroud.)

It is clear from Figs. 3(*a–f*) that the experimental trend of the Cm versus λ curves is not well predicted over part of the range of λ considered. This may be due to a change in secondary

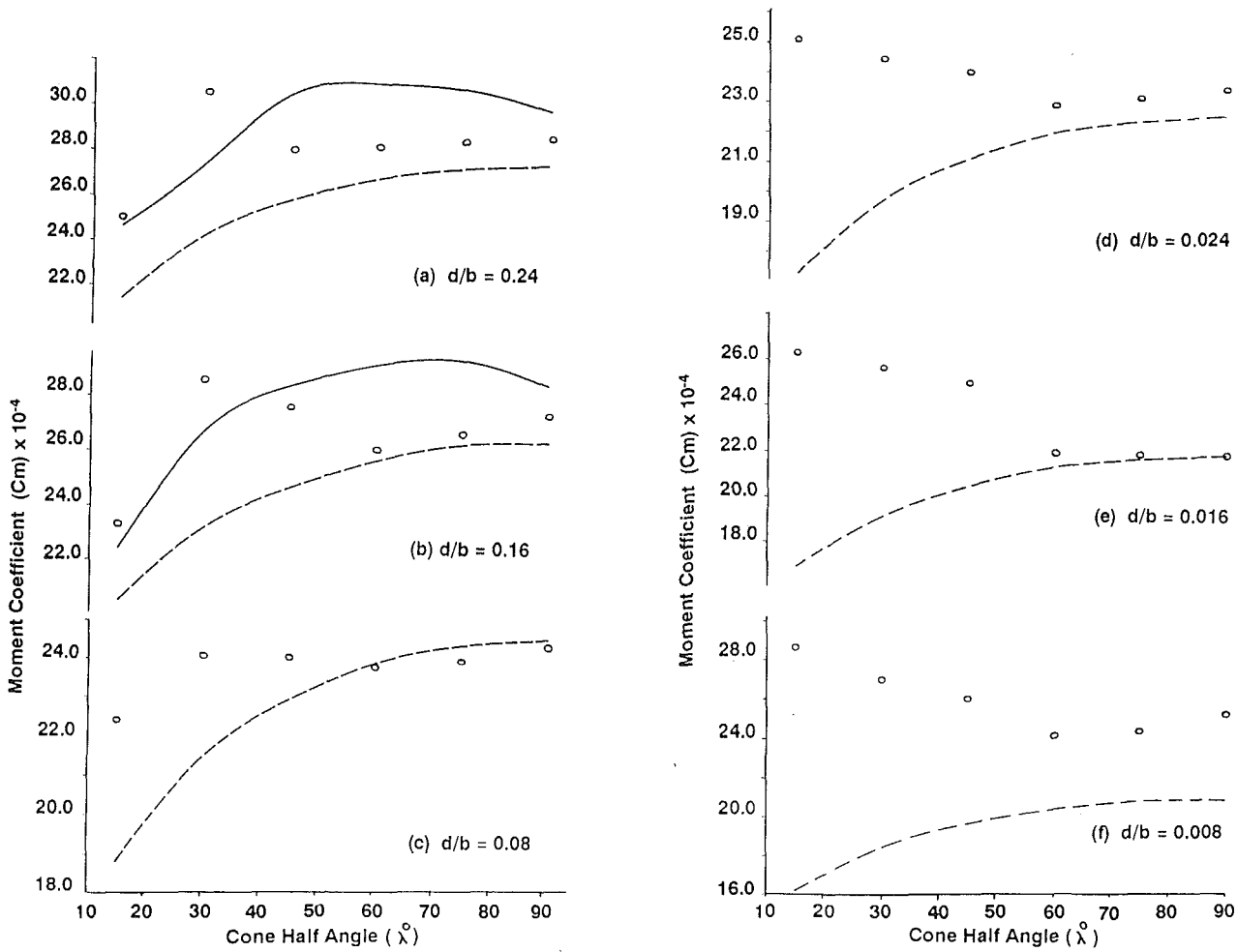

Fig. 3 Comparison of predicted moment coefficients with the data of Yamada and Ito (1975): $C_q = 0$, $a/b = 0$, $\mathrm{Re} = 10^6$ (0 data, —— finite difference, · · · · integral method)

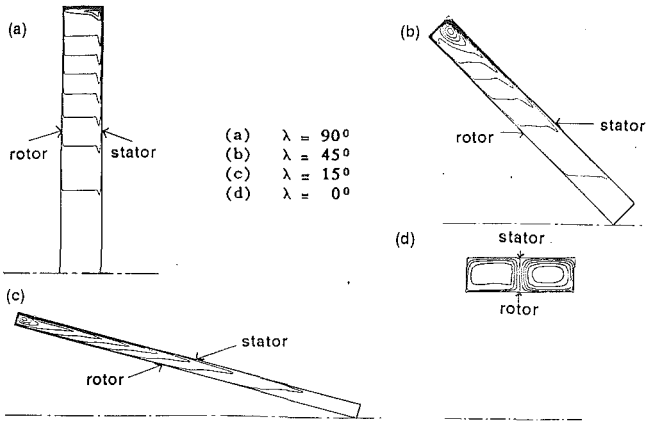

Fig. 4 Streamline predictions for zero throughflow: (*a*)-(*c*): *d*/*b* = 0.16, *a*/*b* = 0, Re = 10^6; (*d*): *d*/*b* = 0.208, *t*/*b* = 0.59, Re = 6.6 × 10^6 (—·—·— axis of rotation)

flow pattern, which is not predicted by the theoretical methods used in this work, occurring at smaller cone half angles. From visual flow studies, Yamada and Ito (1975) report that when $\lambda \geq 60$ deg, any secondary flow will always be of the large-scale "disk-type" as assumed in the integral method. However, for $\lambda \leq 45$ deg, these authors observe that the secondary flow may consist of both the disk-type flow and "Taylor-type" vortices similar to those known to occur in rotor–stator cylinder systems. According to Yamada and Ito, the presence of these vortices, which may be nonaxisymmetric and unsteady, causes an increase in *Cm*, which would explain the experimental trends shown in Figs. 3(*a–f*). While it is clear that the theoretical models cannot be expected to capture large-scale three-dimensional and unsteady effects, it should be noted that there are other assumptions underlying the two models, which might be questioned at low values of λ. These are, first, the assumed forms of the velocity profiles and shear stress laws for the integral method and, second, the mixing-length turbulence model for the finite difference method.

Typical predicted streamline plots obtained from the finite difference method, for cases in which there is no throughflow, are shown in Figs. 4(*a–d*). Figures 4(*a–c*) show that the predicted secondary flow is similar to that assumed in the integral method (Fig. 1) and that the Taylor-type vortices reported in experiments are not predicted. However, Fig. 4(*d*) shows that for a rotor–stator cylinder case ($\lambda = 0$ deg, $Re_\theta = 6.6 \times 10^6$, $d/b = 0.208$, $t/b = 0.59$), the finite difference method predicts two distinct vortices in the secondary flow. For this case the predicted moment coefficient (Cm') of 2.50×10^{-3} compares well with the value of 2.59×10^{-3} given by the empirical correlation of Bilgen and Boulos (1973). Of course, it should not be assumed that the finite difference method predicts the correct velocity field for $\lambda = 0$, but the level of agreement between the moment coefficients is certainly encouraging.

The effect of Reynolds number on *Cm* is shown in Figs. 5(*a–c*). As is to be expected from the above discussion, the agreement between prediction and measurement for $\lambda = 30$ deg shown in Fig. 5(*c*) is generally poor. Figures 5(*a*) and 5(*b*) show good agreement between the integral method predictions and measurement for $Re \geq 2 \times 10^5$. While the results of the integral method and finite difference method agree closely at high Reynolds numbers there is some discrepancy as the Reynolds number decreases. A slight overprediction of moment coefficient at low Reynolds numbers using the present mixing-length turbulence model is consistent with earlier disk cavity studies.

The effect of throughflow rate, *Cq*, on *Cm* is shown in Figs. 6(*a–c*). The figures show that the agreement between theory and experiment generally improves a little as the throughflow

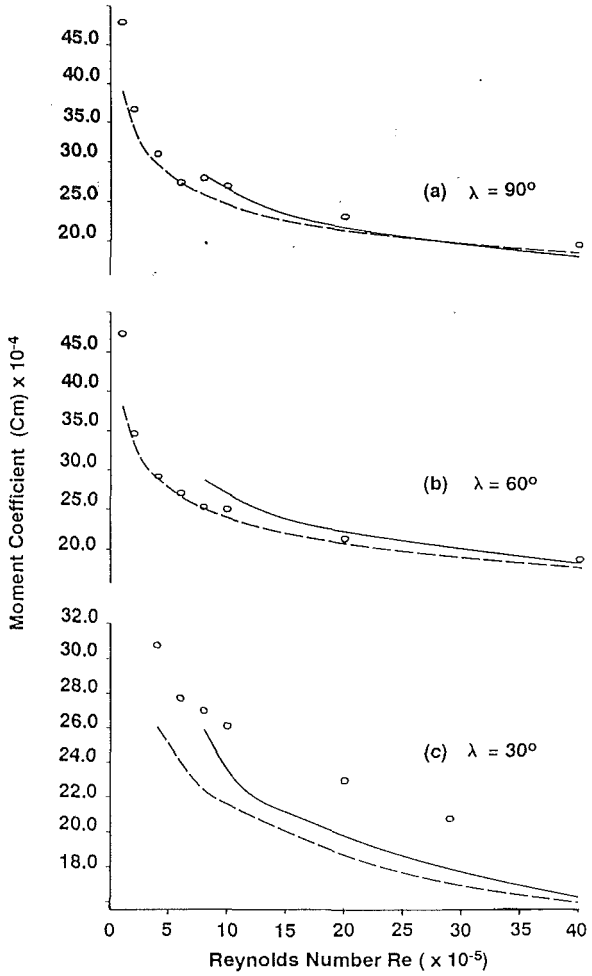

Fig. 5 A comparison of predicted moment coefficients with the data of Yamada and Ito (1975): *Cq* = 0, *a*/*b* = 0, *d*/*p* = 0.8 (○ data; —— finite difference; ···· integral method)

rate is increased. This is, perhaps, to be expected from the results of Yamada and Ito (1979) who found that if, for a particular case with no throughflow, Taylor-type vortices were expected in the secondary flow, then the application of throughflow suppresses their formation.

5 Conclusions

The following conclusions may be drawn from the present study of rotor–stator cone systems:

(*i*) For systems where $\lambda \geq 60$ deg, the integral method moment coefficient predictions are in excellent agreement with experiment. The finite difference predictions are in good agreement and discrepancies for $\lambda = 60$ deg and $\lambda = 75$ deg may be attributable to differences between the geometry of the experimental apparatus and the numerical solution domain.

(*ii*) The experimentally measured increase in moment coefficient as λ decreases is not reproduced by either predictive method. This discrepancy may be due to Taylor-type vortices being present in the flow, which are not predicted by the finite difference method because they are nonaxisymmetric and/or unsteady. For 15 deg $\leq \lambda \leq$ 45 the finite difference predictions for moment coefficient are closer to the measured values than those of the integral method but, over the full range of values of λ considered, the performance of both methods is similar.

(*iii*) The finite difference method predicts the same secondary flow pattern as assumed in the integral method for conical systems where $\lambda \geq 15$ deg. The finite difference results also indicate that the assumptions made in the stator model,

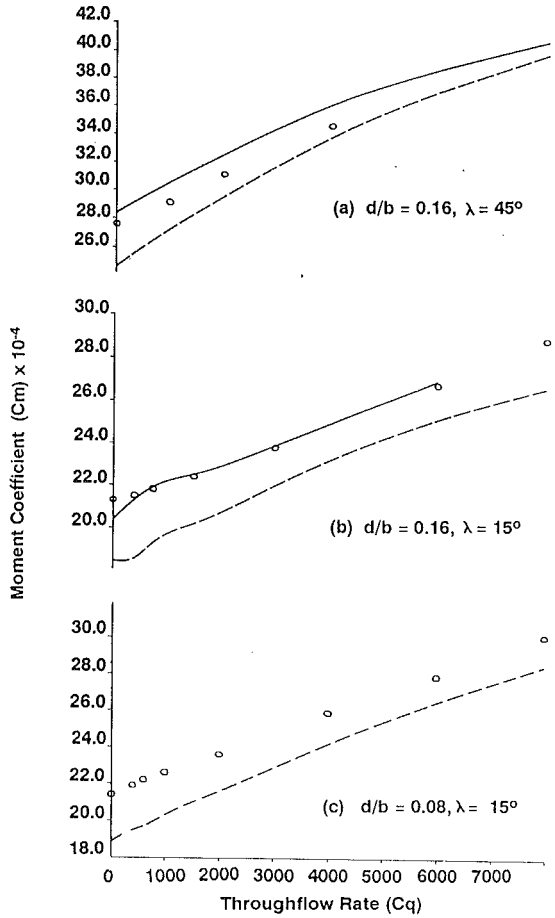

Fig. 6 A comparison of predicted moment coefficients with data of Yamada and Ito (1979): a/b = 0, Re = 10^6 (○ data; —— finite difference; · · · · integral method)

originally for rotor–stator disk systems, may be generalized to conical systems. For the limiting case of a rotating cylinder (λ = 0 deg) the flow structure is quite different. For this case, moment coefficient predictions from the finite difference method are in good agreement with experiment.

(iv) In addition to providing accurate predictions for $\lambda \geq$ 60 deg, the speed of the integral method should be stressed. Comparing a typical computer processing time of tens of seconds with the several hours taken by the finite difference method shows that the integral method does provide an attractive design aid.

Acknowledgments

The authors would like to thank Dr. Craig Vaughan for his assistance with the finite difference coding. The financial support of the Science and Engineering Research Council (UK), and Rolls-Royce plc, via a CASE Studentship, is also gratefully acknowledged.

References

Bilgen, E., and Boulos, R., 1973, "Functional Dependence of Torque Coefficient of Coaxial Cylinders on Gap Width and Reynolds Number," ASME *Journal of Fluids Engineering*, Vol. 95, p. 122.

Chew, J. W., 1985, "Prediction of Flow in a Rotating Cavity With Radial Outflow Using a Mixing-Length Turbulence Model," *Proc. Int. Conf. Lam. and Turb. Flow*, Pineridge, Swansea, United Kingdom.

Chew, J. W., and Rogers, R. H., 1988, "An Integral Method for the Calculation of Turbulent Forced Convection in a Rotating Cavity With Radial Outflow," *Int. J. Heat Fluid Flow*, Vol. 9, p. 37.

Chew, J. W., and Vaughan, C. M., 1988, "Numerical Predictions for the Flow Induced by an Enclosed Rotating Disc," ASME Paper No. 88-GT-127.

Chew, J. W., 1990, "Prediction of Rotating Disc Flow and Heat Transfer in Gas Turbine Engines," *Proc. 3rd Int. Symposium of Transport Phenomena and Dynamics of Rotating Machinery*, Honolulu, HI.

Chew, J. W., 1991, "A Theoretical Study of Ingress for Shrouded Rotating Disk Systems With Radial Outflow," ASME JOURNAL OF TURBOMACHINERY, Vol. 113, pp. 91–97.

Daily, J. W., and Nece, R. E., 1960, "Chamber Dimension Effects on Induced Flow and Frictional Resistance of Enclosed Rotating Discs," ASME *Journal of Basic Engineering*, Vol. 82, p. 217.

Daily, J. W., Ernst, W. D., and Asbedian, V. V., 1964, "Enclosed Rotating Discs With Superposed Throughflow," Report No. 64, Hydrodynamics Lab., Massachusetts Inst. Tech., Cambridge, MA.

Farthing, P. R., Chew, J. W., and Owen, J. M., 1991, "The Use of Deswirl Nozzles to Reduce the Pressure Drop in a Rotating Cavity With a Radial Inflow," ASME JOURNAL OF TURBOMACHINERY, Vol. 113, pp. 106–114.

Kreith, F., 1966, "Frictional Drag and Convective Heat Transfer of Rotating Cones in Mixed and Turbulent Flow," *Proc. Heat Trans. and Fluid Mech. Inst.*, Stanford University Press, p. 29.

Koosinlin, M. L., Launder, B. E., and Sharma, B. I., 1974, "Prediction of Momentum, Heat and Mass Transfer in Swirling Turbulent Boundary Layers," ASME *Journal of Heat Transfer*, Vol. 96, p. 204.

May, N. E., 1990, "Prediction of the Flow and Heat Transfer Between a Rotating and a Stationary Cone," Ph.D. Thesis, Polytechnic South West, Plymouth, United Kingdom.

Morse, A. P., 1988, "Numerical Prediction of Turbulent Flow in Rotating Cavities," ASME JOURNAL OF TURBOMACHINERY, Vol. 110, p. 202.

Morse, A. P., 1991, "Application of a Low Reynolds Number k–ϵ Turbulence Model to High-Speed Rotating Cavity Flows," ASME JOURNAL OF TURBOMACHINERY, Vol. 113, pp. 98–104.

Owen, J. M., Pincombe, J. R., and Rogers, R. H., 1985, "Source-Sink Flow Inside a Rotating Cylindrical Cavity," *J. Fluid Mech.*, Vol. 155, p. 233.

Owen, J. M., and Rogers, R. H., 1989, *Fluid Flow and Heat Transfer in Rotating Disc Systems, Vol. 1; Rotor-Stator Systems*, Research Studies Press, Taunton, United Kingdom.

Patankar, S. V., 1980, *Numerical Heat Transfer and Fluid Flow*, McGraw-Hill, London, United Kingdom.

Roscoe, D. V., Buggeln, R. C., Foster, J. A., and McDonald, H., 1988, "A Numerical Investigation of Fluid Flow for Disc Pumping Applications," ASME Paper No. 88-GT-299.

Tien, C. L., 1960, "Heat Transfer by Laminar Flow From a Rotating Cone," ASME *Journal of Heat Transfer*, Vol. 82, p. 252.

Van Doormal, J. P., and Raithby, G. D., 1984, "Enhancements of the SIMPLE Method for Predicting Incompressible Fluid Flows," *Num. Heat Trans.*, Vol. 7, p. 147.

Vaughan, C. M., Gilham, S., and Chew, J. W., 1989, "Numerical Solutions of Rotating Disc Flows Using a Non-linear Multigrid Algorithm," *Proc. 6th Int. Conf. Num. Meth. Lam. and Turb. Flow.*, Pineridge Press, Swansea, p. 63.

von Karman, T., 1921, "Uber laminare und turbulente Reibung," *Z. angeur. Math. Mech.*, Vol. 1, p. 233.

Yamada, Y., and Ito, M., 1975, "On the Frictional Resistance of Enclosed Rotating Cones," *Bulletin of the JSME*, Vol. 18, No. 123, p. 1026.

Yamada, Y., and Ito, M., 1979, "Frictional Resistance of Enclosed Rotating Cones With Superposed Throughflow," ASME *Journal of Fluids Engineering*, Vol. 101, p. 259.